Wind Turbine Blade Radar Signatures in the Near-Field: Modelling and Experimental Confirmation

Manuel Crespo-Ballesteros, Michail Antoniou, Mikhail Cherniakov
Microwave Integrated Systems Laboratory (MISL)
Department of Electronic, Electrical and Systems Engineering
University of Birmingham
Birmingham, United Kingdom
m.antoniou@bham.ac.uk

Abstract— This paper presents methods and results in modelling wind turbine dynamic radar signatures in the near-field. The theoretical analysis begins with the simpler case of modelling wind turbine blades as rectangular plates. The theoretical radar signature for the wind turbine in the near-field is formulated and its main peculiarities are investigated. Subsequently, the complex shape of the blades is considered and the corresponding radar signatures are modelled. Theoretical modelling is confirmed for both cases via experimental testing in laboratory conditions. It is shown that the experimental results are in good accordance with the theoretically predicted signatures.

***Index Terms*—wind turbine monitoring, Doppler radar**

I. Introduction

The interaction between radar and wind turbines (WTs) has drawn the increased attention of researchers for a number of years. These structures introduce strong radar clutter which affects the operation of radars in surveillance, air and maritime traffic control, weather monitoring, etc. [1]-[7], which may be located several km from a wind farm site. For this reason, the radar research community has dedicated substantial efforts in understanding and mitigating WT radar returns. References [8]-[10] are examples of the work done in numerical modelling of turbines that analyse the effects of the wind farms to the radar and navigation systems performance. Investigations [11]-[18] use experimental data to study WTs radar cross-section (RCS) and investigate methods to mitigate it. Finally, [19]-[23] are examples of research focused on the suppression of WT radar returns through signal processing.

Another common factor in such work is that it usually considers that the radar is in the far-field of the WT blades, meaning that the distance between the radar sensor and the WT is significantly

longer than the length of its blades. In the majority of traditional radar applications (such as surveillance), where WT's are regarded as clutter, this assumption may well hold.

However, this paper takes a different view of the WT/radar interaction, where the above assumption cannot be made. Rather than treating a WT as radar clutter, it is instead considered as a radar target. The reasoning behind this is that radar signatures obtained by WT blades in motion, presumably analysed in the time-frequency (or micro-Doppler) domain, may contain information on their structural integrity. Therefore, rather than suppressing them, it may be possible to analyse them instead to detect or possibly classify their type of fault automatically.

One of the major motivations for considering such a system is that WTs rapidly increase in size and complexity [24]. This means that of course radar clutter becomes more problematic, but also implies that these large structures become increasingly more difficult and expensive to maintain [25]. To tackle the latter problem, WTs currently employ a number of different sensors, installed directly on their blades, and operating at different physical principles (e.g. accelerometers, strain gauges, displacement sensors etc) to persistently monitor WT's unattended and detect different structural faults [26]-[28]. The problem with this approach is that a number of these sensors are required for each blade. For example, only displacement sensors should be spaced by typically 1 m along a blade [29]. With wind turbine blade lengths currently up to 130 m, such methods become increasingly inefficient. On the other hand, a radar sensor with a broad coverage could monitor larger segments of a blade compared to traditional sensors, while at the same time operating at entirely different physical principles. In addition, as it is based on reflections from the WT blades, it may directly measure issues such as blade erosion or build-up of ice, which is currently difficult with existing monitoring tools.

A conceptual radar system that may ultimately be used for this purpose is shown in Fig. 1. It involves a compact, short-range Doppler radar secured on the body (presumably the tower or the nacelle) of the WT. The system has a low-gain antenna illuminating a large part (or the whole) of a WT blade. The sensor can then analyse returns from the blades in motion to identify potential

structural faults.

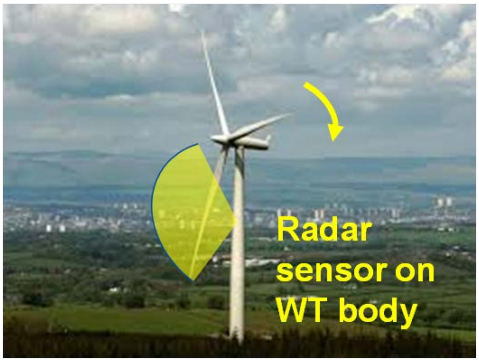

Fig. 1: The concept of compact radar sensors for WT structural monitoring.

At the same time, as a new system concept the appropriate feasibility study should be conducted, where a number of fundamental issues should be understood and solved. So far, it has been experimentally demonstrated that such a system can automatically classify different types of major blade faults [30]. The next problem to consider is an understanding of the radar signatures recorded by the sensor as the blades rotate, i.e. how they vary in the time and time-frequency domain. This is because if an understanding of how the corresponding radar signatures relate to physical aspects of healthy blades and their motion could be obtained, this could be the reference point for identifying faulty blades. Our interest lies on micro-Doppler signatures rather than RCS since it may be more sensitive to blade faults.

Nevertheless, as the distance between the sensor and a blade is now comparable to the length of the blade, the sensor operates in the near-field of the WT. This means that not only current far-field models do not hold [31]-[32], but also the complex shape of the blades becomes more significant. Furthermore, in published work on radar reflections from WTs (see [3], [9], [10] and [33]), a common practice is to use CAD models of WT blades in commercial electro-magnetic (EM) simulators to determine their RCS in static conditions. Although such practice is technically possible here for near-field simulations, it was not preferred for a number of reasons. First of all, the objective of this paper is to model the Doppler signature of WT blades as they rotate, rather than their RCS. Secondly, the final goal of our research is to use dynamic behaviours derived here as a model for characterising faulty blades, where computationally expensive EM simulations could well

turn out to be impractical. The concepts described in this paper, therefore, could be potentially extended to monitor the dynamic behaviour of other rotating mechanical parts in the near-field, such as helicopter rotor blades, for example.

The aim of this paper is to derive models for healthy WT blade signatures in the near-field and analyse them so that this knowledge can be directly applied to our system concept or similar. Both the time domain and joint time-frequency domain signatures are extracted. A theoretical model for the simpler case where blades are assumed to be flat plates is presented in the first part of Section II. In the second part, the more realistic scenario that takes into account the complex shape of the blades is considered. Section III describes an experimental setup in laboratory conditions to verify theoretical modeling, and experimental results are compared to the theoretical expectations.

II. Theoretical Model

A. Flat blades

As a first step, WT blades are assumed flat, whose brief analysis was first considered in [34]. Regarding to the broader radar system parameters, the transmitted signal is a monotonic waveform, transmitted continuously (CW mode), as the intended system is a compact, low-cost Doppler radar (Section I). The radar antenna size is low-gain and is of the order of the radar wavelength, λ. This means that its far-field begins at a few wavelengths and therefore, over small, localised regions of the WT blade, the incident field may be considered a plane wave whose time dependence is $e^{-j\omega t}$. This assumption should be valid in practice, as it is envisaged that the radar sensor is mounted on the body of the WT and therefore its distance from the blades would be in the order of several meters.

This method models a WT blade as a group of scattering centres (Fig. 2). It considers the received signal from each individual point in the WT as the time-shifted replica of the transmitted signal, that is

$$s_R(t) = s_T\big(t - t_r(t)\big) = e^{j\omega_0\left(t - t_r(t)\right)} = s_T(t) \cdot e^{-j\omega_0 t_r(t)} \tag{1}$$

where the time delay is defined by $t_r(t) = 2r\,(t)/c$ and $r(t)$ is the distance to the radar from a point-scatterer.

The overall return from the body is then the coherent sum of all individual signal returns. This first model is used as a stepping stone in understanding the dynamics of the radar signature of a wind turbine in the near-field, as well as the relationship to the its mechanical properties [34]. It is further noted that multi-bounce, diffraction or WT tower structure effects are not taken into account here. The radial distance $r_{q,nm}(t)$ from a single point on the q-blade ($q = 1,2,3$) to the radar is given by:

$$r_{q;nm}(t) = \sqrt{R_N^2 + L_{nm}^2 + 2L_{nm}Z_N cos\left[\Omega t + \alpha_{nm} + \frac{2\pi}{3}(q-1)\right]} \tag{2}$$

where all the parameters included are showed in Fig. 2. The relative height between the radar and the wind turbine is Z_N. The position of a scattering point on the blade is given by l_n and d_m which formed the distance $L_{nm} = \sqrt{l_n^2 + d_m^2}$. The extra angle $\alpha_{nm} = sin^{-1}\frac{d_m}{L_{nm}}$ is added to the phase $\Omega t + \frac{2\pi}{3}(q-1)$. Finally, the radial distance from the radar to the centre of rotation of the hub is given R_N.

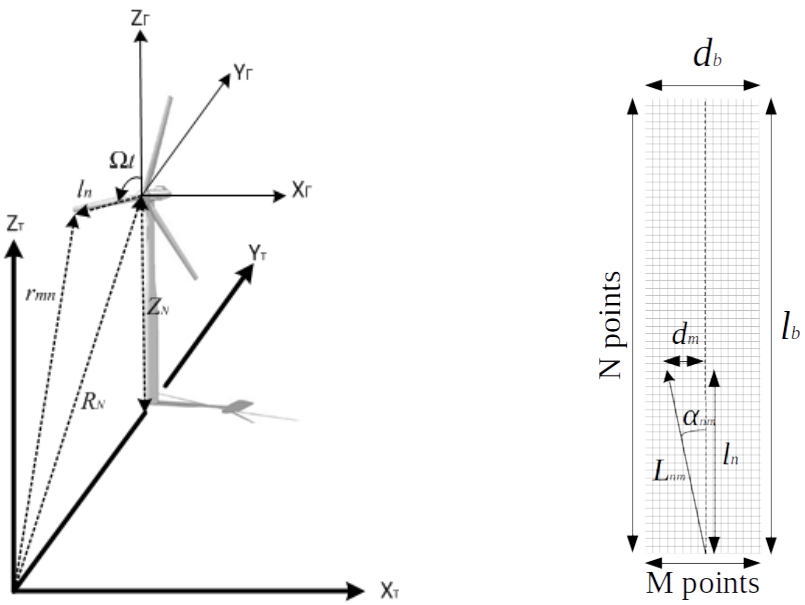

(a) (b)

Fig. 2: (a) Scattering centres model of a rectangular blade. (b) Geometry of the wind turbine/radar system.

Therefore, from expression (1), the signal from a single scattering centre after quadrature demodulation is expressed by:

$$s_{R;qnm}(t) = e^{-j\frac{4\pi}{\lambda}\sqrt{R_N^2+L_{nm}^2+2L_{nm}Z_N cos\left[\Omega t+\alpha_{nm}+\frac{2\pi}{3}(q-1)\right]}} \tag{3}$$

and the full signal of a single blade is given by the addition of all the (n, m) scattering centres:

$$s_{R;q}(t) = \sum_{n=0}^{n=N-1} \sum_{m=\frac{-(M-1)}{2}}^{m=\frac{(M-1)}{2}} e^{-j\frac{4\pi}{\lambda}\sqrt{R_N^2+L_{nm}^2+2L_{nm}Z_N cos\left[\Omega t+\alpha_{nm}+\frac{2\pi}{3}(q-1)\right]}} \tag{4}$$

The literature on the characterisation of WTs radar signature has assumed a far-field approximation for both the transmitted and received signals. This approach neglects the term L_{nm}^2/R_N^2 in equation (4), leading to a $sinc(\cdot)$ form of the backscattered signal. Examples of the work done on WT radar signature using this approach can be seen in [4]. In particular, [4] contains the spectrogram of actual wind turbines and shows the appearance of an inclined flash. As it will be shown, this inclined flash is directly associated to the neglected term in the signal. Fig. 3 compares the signal (4) to the corresponding far-field one. For the sake of comparison, the simulation parameters are very similar to the parameters of an experimental setup within an anechoic chamber (see Section III.A), designed to test theoretical models derived in the paper. These parameters are specified in Table 1.

Simulation parameters of flat blades

Blade length	l_b	0.5 m
Blade width	d_b	0.03 m
Height of the hub respect to the radar	Z_N	0.5 m

Radial distance from the radar to the hub	R_N	3.75 m
Rotational speed	Ω	10 rad/s
Radar transmitting frequency	f_0	24 GHz

Table 1: Parameters of the simulation with flat rectangular blades.

In both cases, two maxima appear over one blade revolution. In the case of the near-field signal, the two maxima are wide and contain a series of maxima and minima before dropping until a flat region at the middle of the signal. The symmetry with respect to the vertical line that passes through the centre of rotation is the reason why two pulses take place in Fig. 3. It can be demonstrated that in the near-field case, the centre of the first of these wide maxima takes place at approximately

$$t_c = \frac{1}{\Omega} cos^{-1}\left(\frac{-l_b}{2Z_N}\right) \tag{5}$$

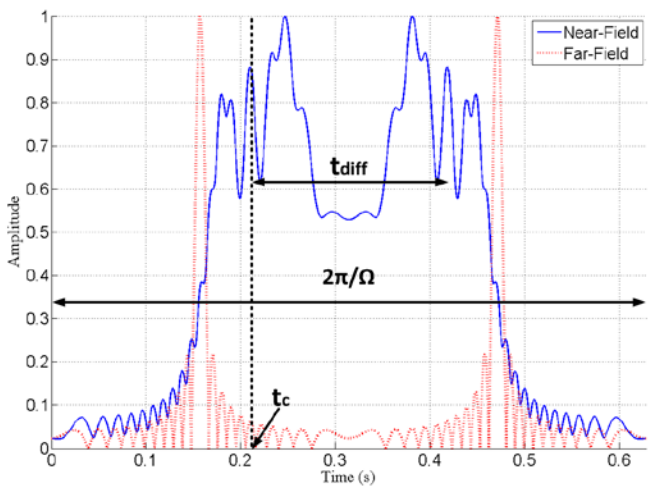

Fig. 3: Far and near field time-domain signature of a single flat blade. The simulation parameters are: $l_b \times d_b = 0.5m \times 0.03m$, $Z_N = 0.5m$, $R_N = 3.75m$, $\Omega = 10\,rad/s$, $f_0 = 24GHz$.

The complete backscattered signal of a wind turbine is the sum of the three blade signals:

$$s_R(t) = \sum_{q=1}^{3} \sum_{n=0}^{n=N-1} \sum_{m=\frac{-(M-1)}{2}}^{m=\frac{(M-1)}{2}} e^{-j\frac{4\pi}{\lambda}\sqrt{R_N^2+L_{nm}^2+2L_{nm}Z_N cos\left[\Omega t+\alpha_{nm}+\frac{2\pi}{3}(q-1)\right]}} \tag{6}$$

One full period $T = \frac{2\pi}{\Omega} s$ of the signal (6) is plotted in Fig. 4. The simulations parameters are the same used in Table 1. It consists of a train of pulses of period $\frac{2\pi}{3\Omega} s$, the time it takes to a blade to sweep the angular shift between two consecutive blades, $\frac{2\pi}{3} rad$.

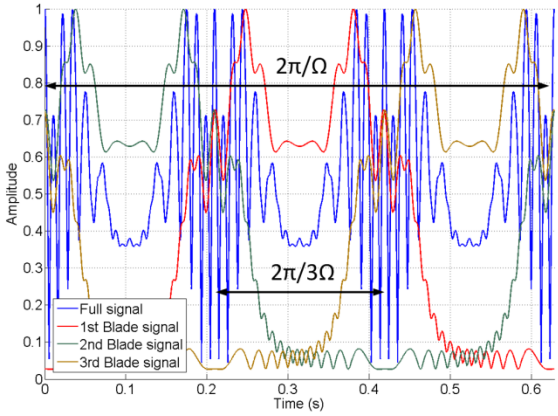

Fig. 4: Time-domain signature over one period of a wind turbine whose blades are modelled as plates. The simulation parameters are: $l_b \times d_b = 0.5m \times 0.03m$, $Z_N = 0.5m$, $R_N = 3.75m$, $\Omega = 10\, rad/s$, $f_0 = 24GHz$.

Fig. 4 also shows that each pulse in the full signal is the combination of two single-blade signals. The explanation for this is geometrically visualized in Fig. 5. The first blade will contribute considerably to the total signal when it is at the angular position Ωt_c, the centre of its first maximum. The second blade will have reached the symmetrical position at a time immediately before. Consequently, the two near individual pulses produce a wide and intense response in the full signal. The contribution of the third blade can be neglected as it is in a position of small signal amplitude. The particular configuration of these pulses will depend on the geometrical parameters of the system.

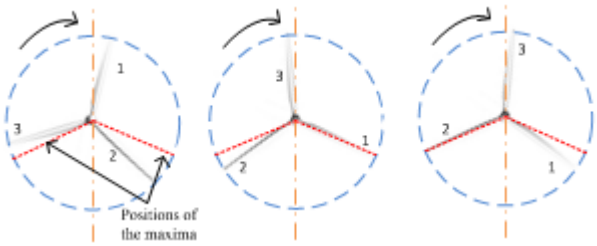

Fig. 5: Positions of maximum backscattered energy.

In order to obtain an analytical expression for the spectrum, the square root in (4) can be approximated by a Taylor series to obtain

$$s_{R;q}(t) = \sum_{n=0}^{n=N-1} \sum_{m=\frac{-(M-1)}{2}}^{m=\frac{(M-1)}{2}} e^{-j\frac{4\pi}{\lambda}\sqrt{R_N^2+L_{nm}^2+2L_{nm}Z_N cos\left[\Omega t+\alpha_{nm}+\frac{2\pi}{3}(q-1)\right]}}$$

$$\cong \sum_{n=0}^{n=N-1} \sum_{m=\frac{-(M-1)}{2}}^{m=\frac{(M-1)}{2}} e^{-j\frac{4\pi}{\lambda}R_N\left(1+\frac{L_{nm}^2}{2R_N^2}+\frac{L_{nm}Z_N}{R_N^2}cos\left[\Omega t+\alpha_{nm}+\frac{2\pi}{3}(q-1)\right]\right)}$$

$$s_{R;q}(t) = \sum_{n=0}^{n=N-1} \sum_{m=\frac{-(M-1)}{2}}^{m=\frac{(M-1)}{2}} C_{nm} e^{jk_{nm}cos\left[\Omega t+\alpha_{nm}+\frac{2\pi}{3}(q-1)\right]}$$

(7)

where $C_{nm} \equiv e^{-j\frac{4\pi}{\lambda}R_N\left(1+\frac{L_{nm}^2}{2R_N^2}\right)}$ and $k_{nm} \equiv -\frac{4\pi L_{nm}Z_N}{\lambda R_N}$. The form of the last expression in (7) allows the invoking of the Jacobi-Anger expression to write

$$s_{R;q}(t) \cong \sum_{n=0}^{n=N-1} \sum_{m=\frac{-(M-1)}{2}}^{m=\frac{(M-1)}{2}} \sum_{p=-\infty}^{\infty} C_{nm}J_p(k_{nm})e^{jp\left[\Omega t+\alpha_{nm}+\frac{2\pi}{3}(q-1)\right]}$$

$$= \sum_{n=0}^{n=N-1} \sum_{m=\frac{-(M-1)}{2}}^{m=\frac{(M-1)}{2}} \sum_{p=-\infty}^{\infty} C_{nm}J_p(k_{nm})e^{jp\alpha_{nm}}e^{jp\frac{2\pi}{3}(q-1)}e^{jp\Omega t}$$

(8)

where J_p are the Bessel functions of first order. By grouping the coefficients that do not depend on time under a single coefficient χ_{nmp}, the signal adopts a simpler form:

$$s_{R;q}(t) \cong \sum_{n=0}^{N-1} \sum_{m=\frac{-(M-1)}{2}}^{m=\frac{(M-1)}{2}} \sum_{p=-\infty}^{\infty} \chi_{nmp} \cdot e^{jp\Omega t} \tag{9}$$

whence it can be concluded that the spectrum of the backscattered signal from a single point on the blade consists of an infinite number of side-band lines at definite frequencies

$$p\Omega - \omega = 0 \leftrightarrow f_p = \frac{\Omega}{2\pi} p \tag{10}$$

where p is the integer of the Jacobi-Anger expansion (8). It is assumed that the radar provides In-phase and Quadrature (I/Q) outputs after mixing the received signal with the carrier frequency f_0, so the actual spectral lines are situated at $f_0 \pm p\frac{\Omega}{2\pi}$. Fig. 6 shows the spectrum calculated after several rotation cycles by applying a Fourier Transform on (4). For the simulation, the exact expression (4) has been used.

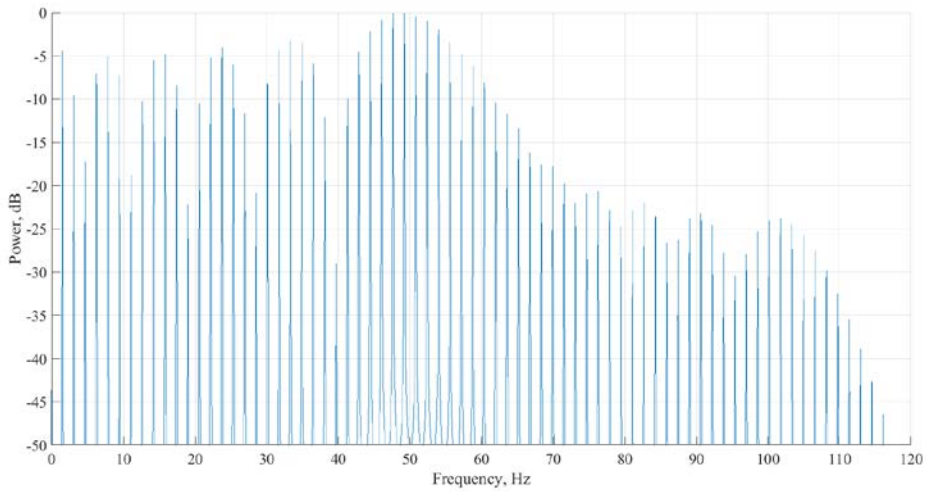

(a)

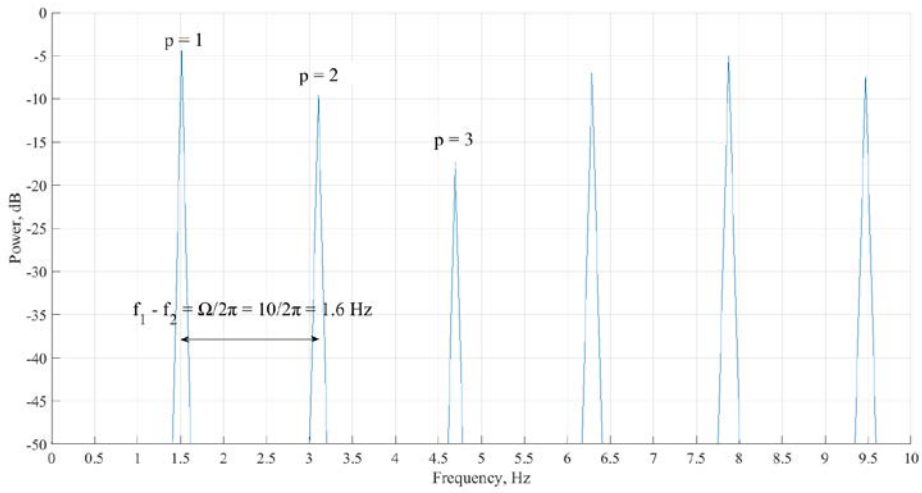

(b)

Fig. 6: (a) One side Spectrum of a single flat blade. (b) Detail of the spectral lines in the spectrum. $\Omega = 10\, rad/s$

The amplitude of the frequencies in the spectrum depends on the Bessel functions $J_p(k_{nm})$. The argument of these functions depend on the value of k_{nm} which ultimately depends on the specific physical parameters of the system wind turbine/radar. If $k_n \ll 1$, which is a far-field situation, only J_0 and $J_{\pm 1}$ are relevant; the spectrum is then formed by few spectral lines. On the other hand, if $k_n \gg 1$, there will be various significant side-band lines. This second case is a near-field situation and the spectrum will be formed by a great number of spectral lines, although the number is finite and the maximum frequency that appear in the spectrum will be related to the velocity of tip.

The joint time-frequency transforms can be used to fully characterise the time-varying frequency content of the signal (6). The best-known of these transformations is the so-called short time Fourier transform (STFT) which consists in dividing the time-domain signal into various segments and take the Fourier transform of each of them [35]-[36]. Its definition is

$$STFT(t,f) = \int s(t')w(t'-t)e^{-j2\pi f t'}dt' \tag{11}$$

The window $w(t)$ selects part of received signal $s(t)$ and calculates its spectrum. The squared magnitude of equation (7) is the so-called spectrogram [37]

$$Spectrogram(t,f) = |STFT(t,f)|^2$$

(12)

Fig. 7 represents the spectrogram of the signal (4); the simulations parameters are those presented in Table 1. It is derived using blocks of data equal to 7680 samples each, using a Gaussian window and a 5% overlap between consecutive blocks. The sinusoidal pattern in the spectrogram corresponds to returns from the blade tip for two revolutions. A bright flash due to the maximum backscattered energy at t_c can be observed and, as it was mentioned, it is inclined and not vertical as the far-field models predicted. Frequencies between $0 - 50Hz$ appear to give stronger echoes than those at higher frequencies. The relative power of the frequencies is related to the spectrum which ultimately depends on the geometrical parameters of the system. For example, in Fig. 6a it can be seen that the power of frequencies higher than $50Hz$ decreases rapidly, as is the case on the spectrogram of Fig. 7. The maximum intensity in the spectrogram takes place at around the mentioned $50Hz$ which correspond to maximum in the spectrum at the same frequency (Fig. 6a).

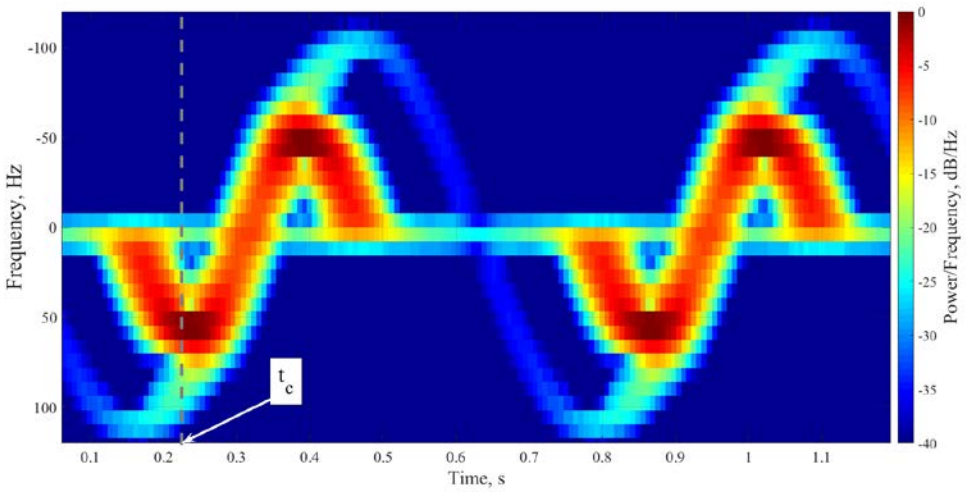

Fig. 7: Spectrogram of a single blade. The simulation parameters are: $l_b \times d_b = 0.5m \times 0.03m$, $Z_N = 0.5m$, $R_N = 3.75m$, $\Omega = 10\,rad/s$, $f_0 = 24GHz$.

B. Curved blades

Having established an understanding of the signature of a flat blade, the analysis can now proceed to the more realistic case. Actual wind turbine blades have a curved contour in order to optimise their aerodynamic functioning [38]. It is this complex shape that determines the scattered

electromagnetic energy.

In the flat blades case, the amplitude of the return wave from a scattering centre is not important in relative terms. All the points lie on the same plane, so there are no major differences in the backscattered energy between nearby scattering centres. This is the reason why, as will be shown in Section III, the scattering centres model accurately represents the experimental signal of a flat blade. That model only takes into account the phase that affects the signal. Therefore, to move to the realistic shape of the blades, it becomes necessary to complete the theoretical framework to include the effects of the amplitude on the backscattered signal.

The typical approach to this problem would have been to use the physical optics approximation $\overrightarrow{J_s} = 2\hat{n} \times \overrightarrow{H_{inc}}$where $\overrightarrow{H_{inc}}$is the incident magnetic field intensity – examples of this method applied to the scattering of a rectangle plate can be found in [39]. In the derivation of the far-field expressions, it is assumed that the far field region begins at $r = 2D^2/\lambda$ where D is the largest dimension of the radiation source, given that D is larger than the wavelength. However, the size of the sources considered here will be several times smaller than the wavelength. Also in this paper, the existence of currents on the blade surface is assumed in first place. The idea is to calculate the fields produced by these currents at the observation point, where the radar is placed. The incident field that induces the surface currents is phase-modulated through the radial distance r that varies with time due to rotating blade surface. This situation differs from the case in [39] where the author assumes a time-harmonic incident field and a static scattering surface. The phase-modulated incident field might be somehow included in this approach, but the calculations would be more complicated and might not have analytic solutions.

The idea of the theoretical framework develop here is to obtain the WT radar signal from EM first principles. This include a detailed understanding of the physics of the problem and aspects like the time varying phase of the incident field through the radial distance. The reasoning presented here recovers the expression (4) (including the 2r/c term typical of the monostatic case) from first principles but with a non constant amplitude.

The assumption of plane wave illumination is still valid. The incident field will excite the charges on the blade surface producing a current density $\overrightarrow{J_S}$ on it. This surface current will have certain amplitude depending on the blade material and the intensity of the incident field. The dependence of time of the current would be $e^{-j\omega t}$ if the blade were not moving. Due to the rotation of the blade, this current density will oscillate in time with a delay given by $\frac{r(t)}{c}$, where $r(t)$ is the radial distance from the radar to a specific point on the blade, that is

$$\vec{J}_s(\vec{x},t) = \vec{J}_s(\vec{x}) \cdot e^{-j\omega\left(t-\frac{r(t)}{c}\right)} \tag{13}$$

where $\vec{x}$are the coordinates of the current density in certain coordinate system. In the case that this system is placed at the centre of rotation, the coordinates $\vec{x}$would be the vector $\vec{L}_{mn}$ already introduced and $r(t) = \left|\vec{R}_N - \vec{L}_{mn}\right|$.

The current density $\overrightarrow{J_S}$can be considered as forming a vector field defined on the 2-D surface S(Fig. 8). In general terms, a vector field on a surface is defined as a smooth map between that surface $S$and the tangent bundle TS (the collection of all tangent spaces at S) with the attribute that for each point P on Sthere is a vector associated that lies in TS_P, the tangent space at P [40]. At each point on S, a vector $\overrightarrow{J_S}$ can be defined on the corresponding tangent plane building thus a vector field which has a physical meaning. For a sufficient smooth surface, as it is the case of the WT blade, the vectors $\overrightarrow{J_S}$ in the neighbourhood of a point P can be considered to lie on the same tangent plane TS_P. Therefore, the blade can be divided into *flat* regions where particular charge and current density distributions are present. These currents are the sources of the electromagnetic fields that produce the total backscattered wave detected by the radar. The linearity of Maxwell's equations guarantees that the total field is the result of the superposition of these individual contributions.

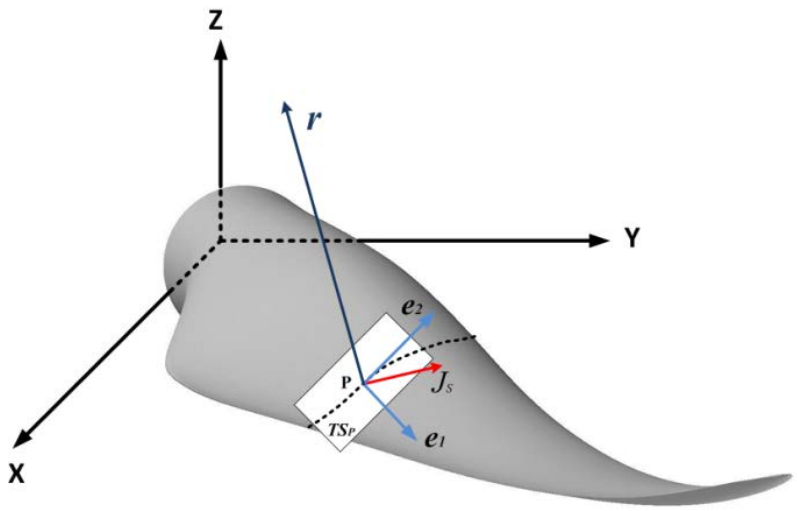

Fig. 8: Current density vector at point P. $\vec{J_S}$ is tangential to the blade surface and lies on the tangent plane TS_P. This current density vector can be expanded by the tangent plane basis $\{\hat{e}_1, \hat{e}_2\}$.

The method suggested in this paper consists on treating each radiating source independently and add them in order to form the total signal at the radar position. Two consequences can be inferred from this idea. On the one hand, a far-field approximation can be assumed as the distance to the observation point is much larger than the size of the individual, elementary sources; the calculations will be thus highly simplified. On the other hand, these calculations can be performed in a 2D Euclidean space instead of dealing with curved surfaces.

The aim now is to build the tangent bundle TSor, more precisely, to construct the individual tangent spacesTS_Pat each point on the blade and associate to each one the corresponding current distribution $\vec{J_S}$. To do this, the tangent plane at any point P, TS_P,is expanded by a basis $\{\hat{e}_1(P), \hat{e}_2(P)\}$ which are the tangent vectors at the blade point P in the x^1, x^2 directions, the generalised coordinates that parametrise the surface as it can be seen in Fig. 9. The normal vector to the surface and the basis vectors are mutually perpendicular. Any vector lying on $TS_P$is a linear combination of the vectors $\{\hat{e}_1(P), \hat{e}_2(P)\}$, so the current density $\vec{J_S}$can be written in terms of this basis. In order to evaluate the resultant fields at the radar position, a global Cartesian coordinates system is placed at the centre of rotation as Fig. 8 shows. The basis $\{\hat{e}_1(P), \hat{e}_2(P)\}$ is defined at each point $P := (x', y', z')$ on the blade given by the vector$\vec{L}_{mn}$. Fig. 9 represents the basis

$\{\hat{e}_1(P), \hat{e}_2(P)\}$ at different points on the blade surface. The orientation of these vectors varies along the profile of the blade.

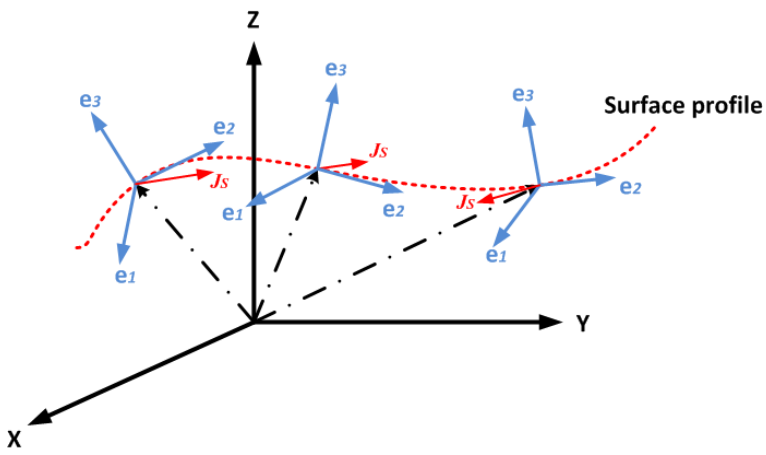

Fig. 9: Vectors of the tangent planes basis at different points along the blade surface.

The electromagnetic fields created by each elementary scattering area can be determined by calculating the vector potential $\vec{A}(\vec{x}, t)$, whose solution in the Lorentz gauge is [41]

$$\vec{A}(\vec{x}, t) = \frac{\mu_0}{4\pi} \int ds' \int dt' \frac{\vec{J_S}(\vec{x}', t')}{|\vec{r}(t) - \vec{x}'|} \delta\left(t' + \frac{|\vec{r}(t) - \vec{x}'|}{c} - t\right) \tag{14}$$

where μ_0 is the permeability of free space. The coordinates $\vec{x}'$ evaluate the charge and current density distributions on the tangent plane TS_P. The vector $\vec{r}(t)$ is the radial distance between the radar and a specific point on the blade and its modulus is $r(t)$. The Dirac delta function δ accounts for the correct time delayed in the signal. The transmitted radar signal will be incident on the blade at a certain angle due to the geometrical configuration of the system and/or the curvature of the WT blade. Therefore, the signal will reach different points at distinct phases which means that separated parts of the blade will experience different field intensities and orientations. Consequently, a complex charge and current distribution will be induced over the blade. The current amplitude $\vec{J}_s(\vec{x}')$must vary over each flat area considered as a source in order to satisfy the boundary conditions between different regions.

After substituting the current distribution (13) into the vector potential (14), the latter can be

written as

$$\vec{A}(\vec{r}(t),t) = \frac{\mu_0}{4\pi}\int ds' \int dt' \frac{\overrightarrow{J_S}(\vec{x}')e^{-j\omega\left(t'-\frac{r(t)}{c}\right)}}{|\vec{r}(t)-\vec{x}'|}\delta\left(t' + \frac{|\vec{r}(t)-\vec{x}'|}{c} - t\right)$$

(15)

Any disturbance in the radiated electromagnetic fields will propagate at c, so the propagation time is approximately in the order of $t_d = \frac{r}{c}10^{-8}s$. The variation in the charge and current density distributions due to the rotation of the blade is of the order of $t_r = \frac{1}{\Omega}10^{-1}s$. Therefore, the elementary sources are practically static during the propagation of the electromagnetic fields. Once the radial distance $r(t)$ is known for each point, the current density in (13) can be considered as an independent radiating source that oscillates deterministically in time producing electric and magnetic fields that propagate through space. Therefore, the radial distance enters into the equation (15) just depending on the time t and no extra delay is necessary to take into account inside $r(t)$.

After evaluating the delta function in equation (11), the vector potential is given by

$$\vec{A}(\vec{r}(t),t) = \mu_0 e^{-j\omega\left(t-\frac{r(t)}{c}\right)}\int ds' \overrightarrow{J_S}(\vec{x}')\frac{e^{-jk|\vec{r}(t)-\vec{x}'|}}{4\pi|\vec{r}(t)-\vec{x}'|}$$

(16)

The so-called Green's function

$$G(\vec{r}(t),\vec{x}') \equiv \frac{e^{-jk|\vec{r}(t)-\vec{x}'|}}{4\pi|\vec{r}(t)-\vec{x}'|}$$

(17)

can be introduced in order to write the vector potential (12) as

$$\vec{A}(\vec{r}(t),t) = \mu_0 e^{-j\omega\left(t-\frac{r(t)}{c}\right)}\int ds' \overrightarrow{J_S}(\vec{x}')G(\vec{r}(t),\vec{x}')$$

(18)

The fields are given only in terms of the spatial derivatives of $\vec{A}(\vec{r}(t),t)$, so the phase $e^{-j\omega t}$can be ignored in the subsequent calculations. This will lead to an expression of the backscattered electric field whose phase is the one predicted by the SCM and the amplitude will depend on the

point of the blade and its orientation respect to the radar position.

The exact expansion of the Green function $G(\vec{r},\vec{x}')$ for points outside the source allows writing the vector potential (18) in spherical coordinates as [41]

$$\vec{A}(\vec{r}) = j\mu_0 k e^{jkr} \sum_{l,m} h_l^{(1)}(kr) Y_{lm}(\theta,\varphi) \int ds' \vec{J_s}(\vec{r}') j_l(kr') Y_{lm}(\theta',\varphi') \tag{19}$$

where the dependence with time of the observation position has been omitted to simplify the notation and $k = \omega/c$. The terms $h_l^{(1)}(kr)$ and $j_l(kr')$ are the spherical Hankel and Bessel functions and $Y_{lm}(\theta,\varphi)$ are the so-called spherical harmonics. If only the first term $l = 0$ (and $m = 0$) of the series (19) is retained, the vector potential becomes

$$\vec{A}(\vec{r}) = j\mu_0 k e^{jkr} \left[h_0^{(1)}(kr) Y_{00}(\theta,\varphi) \int ds' \vec{J_s}(\vec{x}') j_0(kr') Y_{00}(\theta',\varphi') \right] \tag{20}$$

The isotropic spherical harmonics are

$$Y_{00}(\theta,\varphi) = Y_{00}(\theta',\varphi') = \frac{1}{\sqrt{4\pi}} \tag{21a}$$

On the other hand, the Hankel and Bessel functions corresponds to

$$h_0^{(1)}(kr) = \frac{e^{ikr}}{jkr} \tag{21b}$$

$$j_0(kr') = \frac{sinkr'}{kr'} \tag{21c}$$

Expression (21c) can be in general approximated by $sinc(kr') \approx 1$ as the maximum value of the source size r' is several times smaller than the wavelength. This approximation will be as closer to 1as the size of the source decreases. This will depend on the incident angle of the transmitted field. In the present case of study, the maximum value of r' is of the order of $\lambda/6$ which gives a range for

the value of (21c) of $0.86 - 1$. In order to obtain an analytical expression for the integral (20) and to avoid interpolating the measured points, the Bessel function will be approximated by 1. There is missing information since this approximation is equivalent to consider a smaller source without filling the gap between two measured points by interpolating an extra source. However, the comparison between theoretical and experimental results will validate the appropriateness of this assumption.

Introducing the expressions (21a)-(21c) in (20), the vector potential can be written as

$$\vec{A}(\vec{r}) = \frac{\mu_0}{4\pi}\frac{e^{j2kr}}{r}\int ds'\vec{J_s}(\vec{r}') \tag{22}$$

This last expression of the vector potential can also be obtained by setting $|\vec{r}(t) - \vec{x}'| = r$ in (16).

The dependence of $\vec{A}(\vec{r})$ only on the radial distance implies that the electromagnetic fields will depend on r as well. Any angular dependence will appear as a result of the cross-products necessary to calculate $\vec{E}(\vec{r})$ and $\vec{B}(\vec{r})$. Furthermore, due to fact that the vector potential rolls off as r^{-1} (22), the fields will present the same behaviour as expected in the radiation zone (higher orders will be discarded).

The expression for the current distribution is not known, so the surface integral in (18) cannot be calculated analytically. However, the integral can be written

$$\vec{A}(\vec{r}) = \frac{-\mu_0}{4\pi}\frac{e^{j2kr}}{r}\int ds'\vec{x}'\left(\nabla\cdot\vec{J_s}(\vec{x}')\right) \tag{23}$$

which suggests the use of the continuity equation: $\nabla\cdot\vec{J_s} = \frac{-\partial\rho}{\partial t}$. As it was already mentioned, the incident electric field creates a complex charge and current distribution over the blade. The charge distribution, as in the case of the current in (13), will have the form

$$\rho(\vec{x}', t) = \rho(\vec{x}')e^{-j\omega\left(t-\frac{r(t)}{c}\right)} \tag{24}$$

Using these distributions, the continuity equation becomes

$$\nabla \cdot \left[\vec{J_s}(\vec{x}')e^{-j\omega\left(t-\frac{r(t)}{c}\right)}\right] = \frac{-\partial}{\partial t}\left[\rho(\vec{x}')e^{-j\omega\left(t-\frac{r(t)}{c}\right)}\right]$$

(25)

Notice though that the spatial derivatives are performed on the source coordinates $\vec{x}'$ and do not affect the radial distance in the exponential. Consequently, after ruling out the common exponential, expression (25) can be written

$$\nabla \cdot \vec{J_s}(\vec{x}') = j\omega\rho(\vec{x}')\left(1 + \frac{\Omega L_{mn} Z_N}{c}\frac{sin\Omega t}{r(t)}\right)$$

(26)

Substituting the divergence of the current distribution in expression (23), the vector potential becomes

$$\vec{A}(\vec{r}) = \frac{-\mu_0}{4\pi}\frac{e^{j2kr}}{r}\int ds'\vec{x}'j\omega\rho(\vec{x}')\left(1 + \Omega L_{mn} Z_N \frac{sin\Omega t}{cr}\right)$$

$$= -j\frac{k}{4\pi c\varepsilon_0}\frac{e^{j2kr}}{r}\vec{p}\left(1 + \Omega L_{mn} Z_N \frac{sin\Omega t}{cr}\right)$$

(27)

where $\vec{p} \equiv \int ds'\vec{x}'\rho(\vec{x}')$ is the electrostatic electric dipole. The second term in parenthesis in expression (27) produces a contribution of order r^{-2}. Since only the radiation contribution to the fields will be considered, those that vary with r^{-1}, a sufficient accurate approximation of the vector field is

$$\vec{A}(\vec{r}) = -j\frac{k}{4\pi c\varepsilon_0}\frac{e^{j2kr}}{r}\vec{p}$$

(28)

The total electric field vector, after recovering the oscillation in time, is derived in the Appendix and finally it can be written as

$$\vec{E}(\vec{r},t) = \frac{3}{2}\frac{k^2}{\pi\varepsilon_0}\frac{(\hat{r}\times\vec{p})\times\hat{r}}{r}e^{-j\omega\left(t-\frac{2r}{c}\right)}$$

(29)

The modulus of the electric dipole $|\vec{p}|$ in (29) would, in principle, depend on the material of the blade surface and the strength of the incident field. The orientation of the dipole will be aligned to the current orientation and this last one possesses the orientation of the electric field. Therefore, the dipole is seen as a vector that slowly rotates on the tangent plane of that specific point and rapidly oscillates with time. On the other hand, as the blade moves, $\hat{r}(t)$ also changes its orientation. Consequently, the movement of the blade produces a time-varying relative angle between the source and the direction of observation. The cross-products in expression (29) take into account only the component that is perpendicular to the line of sight, as it must be. As the relative orientation between $\hat{r}$ and $\vec{p}$ varies, the strength of the backscattered signal will also change.

An expression for the rotation of the dipole is now necessary to complete the theoretical framework. In order to do this, the polarisation of the incident electric field has to be defined. The monostatic radar used for experimental measurements is linearly vertical polarised. Therefore, the dipole will point in the same direction and will rotate on the tangent plane as the blade moves as Fig. 10 shows, and only the vertical component of the field (29) will be taken into account. At this stage it should be stated that a natural extension of the models in this paper could be to consider their full polarimetric implementation.

A rotating dipole can be obtained by superimposing two perpendicular oscillating dipoles. The frequency of oscillation must be the angular velocity of the blade. In order to compare the theoretical expression with the experimental signal, the components of the electric dipole on the tangent plane in terms of the basis vectors$\hat{e}_1(P), \hat{e}_2(P)$ should be, for the specific electric field polarization,

$$\vec{p} = p_0[-sin\Omega t \cdot \hat{e}_1(P) + cos\Omega t \cdot \hat{e}_2(P)]$$

(30)

which is a rotation opposite to the blade spinning. The specific value for p_0 does not affect the final result in relative terms as long as it is the same for all the points.

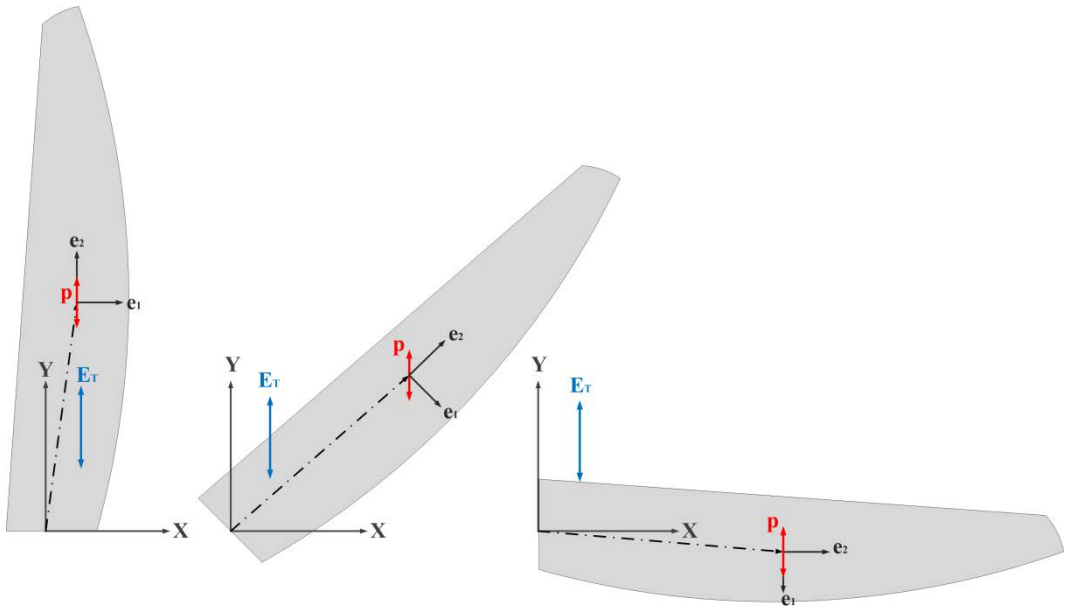

Fig. 10: Orientation of the electric dipole as the blade rotates.

The contribution of all the sources on the blade will produce the total field at the radar position:

$$\vec{E}_{total} = \sum_{\forall n} \vec{E}_n(\vec{r}_n, t) = \frac{3}{2}\frac{k^2}{\pi\varepsilon_0}\sum_{\forall n}\frac{(\hat{r}_n \times \vec{p}_n) \times \hat{r}_n}{r_n} e^{-j\omega\left(t-\frac{2r_n}{c}\right)} \tag{31}$$

The intensity of the total field will change as a result of the different amplitude of the sources at different blade positions. As desired, an expression for the amplitude of the backscattered wave has been obtained.

Expression (4) can be recovered from (31) if, as it was mentioned at the beginning of this section, there are no major differences in the energy backscattered from different parts of a flat blade. This is equivalent to assume that the amplitude in (31) is almost the same for all the points and therefore

$$\vec{E}_{total} = \frac{3}{2}\frac{k^2}{\pi\varepsilon_0}\sum_{\forall n}\frac{(\hat{r}_n \times \vec{p}_n) \times \hat{r}_n}{r_n} e^{-j\omega\left(t-\frac{2r_n}{c}\right)} \approx C \cdot e^{-j\omega\left(t-\frac{2r_n}{c}\right)} \tag{32}$$

The simulation results obtained for curved blades are similar to the flat blades case, although they present particular characteristics. Therefore, the analysis of the radar signature predicted by (32) will be done together with the experimental results in section III which will also show the

justification for developing a more realistic case.

III. Experimental Verification

A. Experimental set-up

Several experiments with scaled WTs were performed in order to confirm the theoretical models. Fig. 11a shows the aluminum flat blades built to verify the theoretical results obtained in section II. The length of each one of the blades is $l_b = 0.5m$ while its width is $d_b = 0.03m$. For the returns from real blades, an off-the-shelf small wind turbine (~0.5m blade length) was used (Fig. 11b). Its blades were covered with aluminum paint to improve their reflectivity.

At this stage it is worth mentioning that this set of experiments does not represent a scaled anechoic chamber experiment in the traditional sense, where there is a scaling ratio between frequency and target size. The reason for this is that at this early stage in the research of the overarching problem of trying to detect WT faults, there is no set recommendation on the frequency to be used (even the 24 GHz considered here could ultimately be used), where at the same time WT blade lengths could vary from a few tens of meters to more than 120m. Instead, the experimental setup was built to test the major objective of this paper, which is the modelling of WT radar signatures in the near field, with a CW radar device and WTs of an appropriate size for the anechoic chamber.

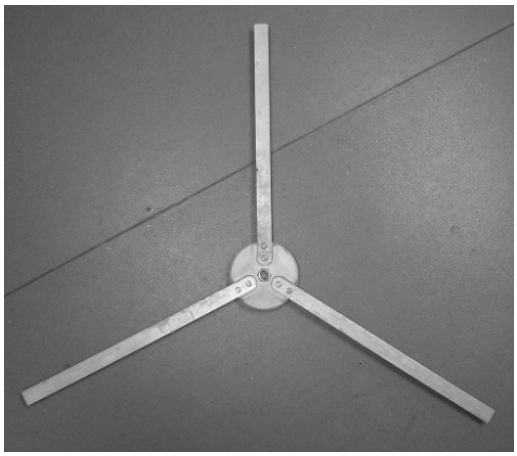

(a)

(b)

Fig. 11: Wind turbine blades used during the experiments: (a) flat blades; (b) curved blades.

During experimentation, the scaled models were placed inside an anechoic chamber where their radar signatures were recorded. To set their rotational velocity at a known value, a DC motor was attached to the the WT. The radar was a 24 GHz Doppler radar with I/Q digital outputs and a sampling frequency of 44.1 kHz, with the unambiguous Doppler range being half the sampling frequency [42]. The experimental set-up is sketched in Fig. 12 and the experimental parameters are listed in Table 2.

Experimental parameters of flat blades

Blade length	l_b	0.5 m
Blade width	d_b	0.03 m
Height of the hub respect to the radar	Z_N	0.5 m
Radial distance from the radar to the hub	R_N	3.7 m
Rotational speed	Ω	Medium velocity: 4.6 rad/s Maximum velocity: 9.4 rad/s
Radar transmitting frequency	f_0	24 GHz

Table 2: Experimental parameters of the experiment with flat rectangular blades.

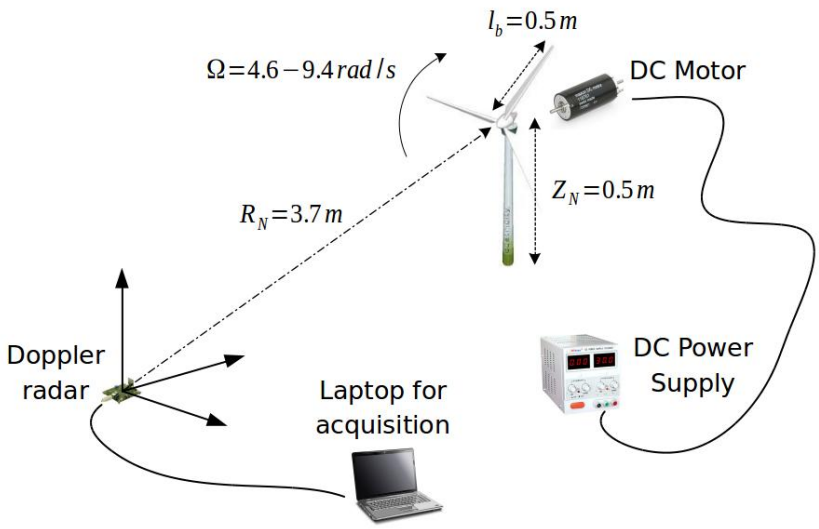

(a)

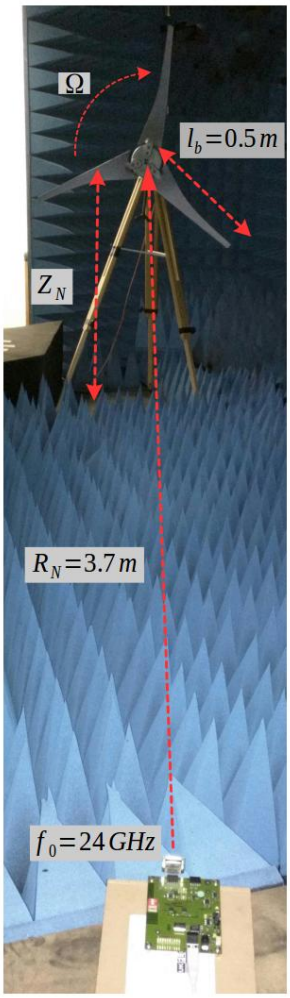

(b)

Fig. 12: (a) Sketch of the experimental set-up. (b) Experimental set-up in the anechoic chamber

In order to compare the experimental signature of the real blades (Fig. 11b) to the theoretical model of Section II, a CAD model of one of the blades was manually created. The system used to obtain the coordinates of different points on the blade is displayed in Fig. 13a. The separation between two points in the x and y direction was $4mm$ maximum which is equivalent to $\lambda/3\,m$. The height or z coordinate was measured with the help of a calliper. The blade surface can then be represented by a set of points with three components: height and directions along and transversal to the blade. The result is shown in Fig. 13b. The expression derived in (29) was applied to each of these points to obtain the theoretical signal. The radar antenna transmits and receives in horizontal polarization, so only the component $E_x$in equation (29) was used to simulate the signal.

A low-pass filter was applied to the recorded radar signatures to remove high frequency noise. Additionally, the Doppler radar contains a Butterworth high-pass filter, so the same filter was applied to the theoretical signals of (4) and (29) for comparison with experimental results. A block diagram of the experimental signal processing is shown in Fig. 14.

The correlation coefficient between the theoretical signature, A, and the experimental one, B, was used to assess the accuracy of the theoretical models. This correlation coefficient is defined as:

$$r_{coeff} = \frac{\sum_m \sum_n (A_{mn} - \acute{A})(B_{mn} - \acute{B})}{\sqrt{\left(\sum_m \sum_n (A_{mn} - \acute{A})^2\right)\left(\sum_m \sum_n (B_{mn} - \acute{B})^2\right)}} \tag{32}$$

where $\acute{A}$ and $\acute{B}$ are the mean value of the signals.

B. Results for flat blades

Fig. 15a shows the comparison between the experimental and theoretical time-domain signatures of a single flat blade. The correlation coefficient between both signatures is 0.92. The experimental signal presents the characteristics predicted by the analysis of equation (4): two symmetric wide peaks forming a train of pulses whose duration is $2\pi/\Omega$s, the rotational period.

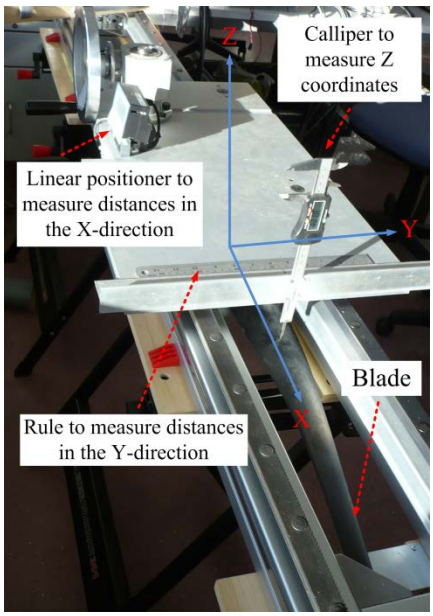

(a)

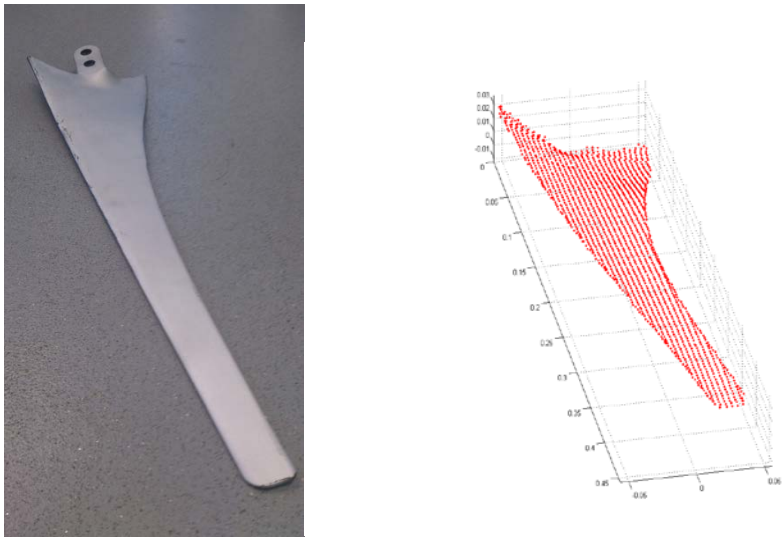

(b)

Fig. 13: (a) Set-up built to measure the blade profile. (b) Real blade and the CAD model obtained.

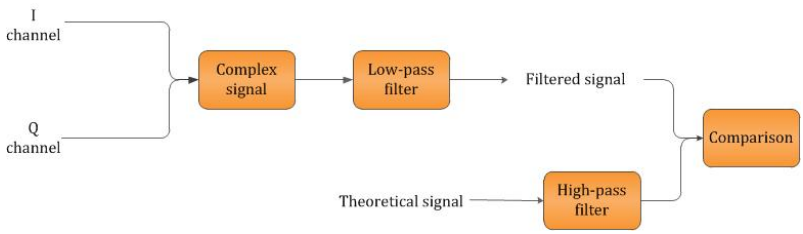

Fig. 14: Block diagram of the methodology used to compare simulations and experimental results.

The dip in both signatures at their centres is due to the high-pass filter of the radar. All plots are

normalized to their respective highest intensity (hence the maximum of 0 dB).

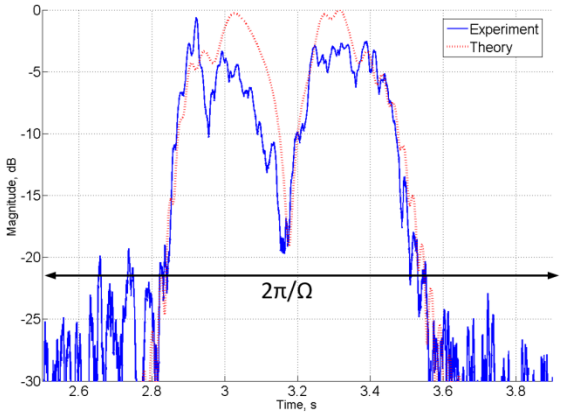

(a)

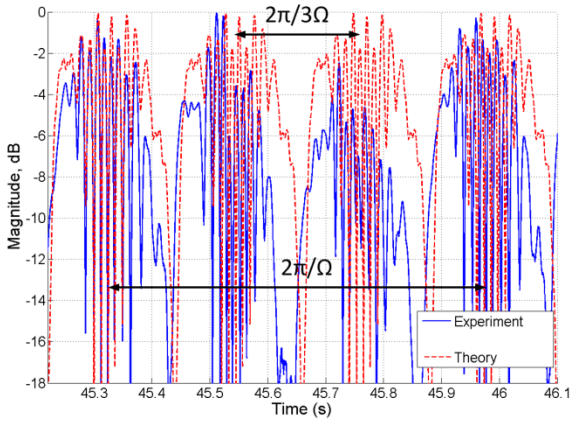

(b)

Fig. 15: Theoretical and experimental time-domain signatures. $l_b \times d_b = 0.5m \times 0.03m$, $Z_N = 0.47m$, $R_N = 3.77m$, , $f_0 = 24GHz$. (a) One blade, Ω=4.6 rad/s; (b) Three blades, Ω=9.4 rad/s

The case of three blades is displayed in Fig. 15b. The features of time-domain signature is also well-predicted by the theoretical model. The correlation coefficient in this case is 0.89. The signal is formed by a train of pulses separated in time $2\pi/3\Omega\, s$, as predicted by the theoretical analysis. As it was described at the beginning of Section II, the individual backscattered signals of two blades combine to form one single return in the three blades signature. Therefore, the inevitable physical differences between the blades themselves produces discrepancies among the returns in the experimental signal. The time-domain signature replicates itself every $2\pi/\Omega\, s$, the period of one full turbine revolution.

The other relevant part of the analysis is the joint time-domain frequency of the signal or micro-Doppler signature. The graphs in Fig. 16 correspond to the theoretical and experimental spectrograms of a single flat blade. From Fig. 16b it can be verified that the period of the signal is that given by the SCM, i.e $T = \frac{2\pi}{\Omega} = \frac{2\pi}{9.4} = 0.668s$. As it was predicted in equation (5), when the blade reaches its position of maximum backscattered energy, the micro-Doppler signature presents an intense response. This instant of time is given by $t_c = \frac{1}{\Omega} cos^{-1}\left(\frac{-l_b}{2Z_N}\right) = 0.227s$. The comparison with the theoretical spectrogram shows that this flash occurs at $45Hz$ approximately and it is inclined. This behaviour has been observed in previous investigations done on WT radar signature, e.g. [4]. In particular, the theoretical approach in [4] consisted in eliminating the term L_{nm}^2/R_N^2 from a similar equation like (6). The paper [4] contains the spectrogram of an actual WT and shows the appearance of an inclined flash. As This phenomenon is directly associated to the neglected term L_{nm}^2/R_N^2. In this research, the SCM reproduce this behaviour when the quadratic term is conserved.

The lower frequencies also exhibits intense level of power as predicted. In the experimental micro-Doppler, the trace of the tip present in the theoretical signature, can also be seen above the 45Hz bright point.

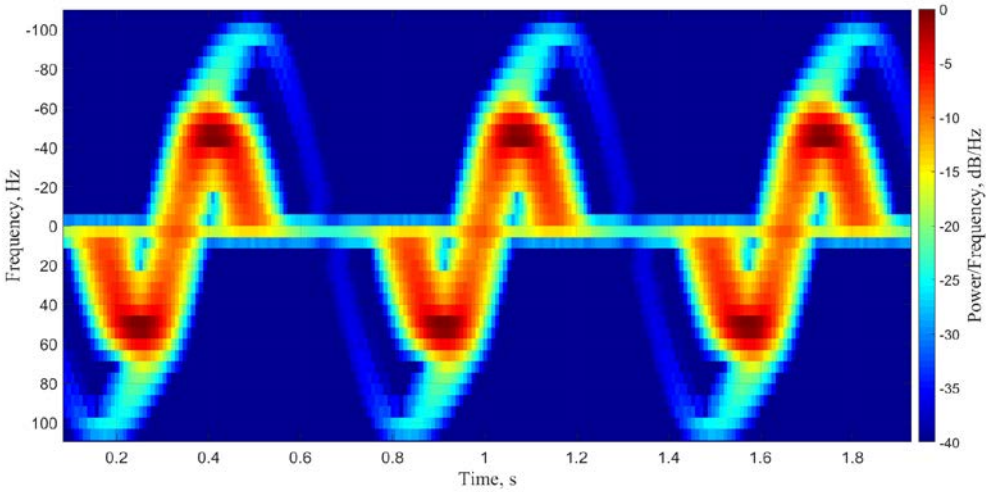

(a)

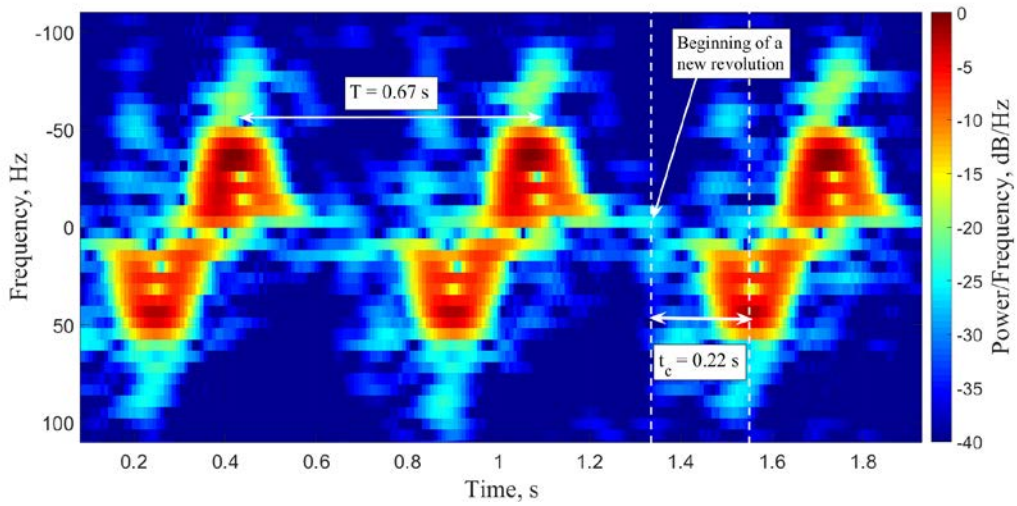

(b)

Fig. 16: Micro-Doppler signature of a single flat blade. $l_b \times d_b = 0.5m \times 0.02m$, $Z_N = 0.47m$, $R_N = 3.77m$, $f_0 = 24GHz$, $\Omega = 9.4\,rad/s$. (a) Theoretical signature; (b) Experimental signature.

Fig. 17 shows the theoretical and experimental spectrograms of the WT. The pattern observed in the case of a single blade (Fig. 16) replicates itself here three times each period. This means that no complicated electromagnetic effects are observed and each blade generates its own individual signature. However, part of the individuals signals overlap on the spectrogram producing a dense graph where the clear sinusoidal trace of Fig. 16 cannot be distinguished. Note that two different rotational velocities have been used to generate Fig. 16 (9.4 rad/s) and Fig. 17 (4.6 rad/s), as defined in Table 1.

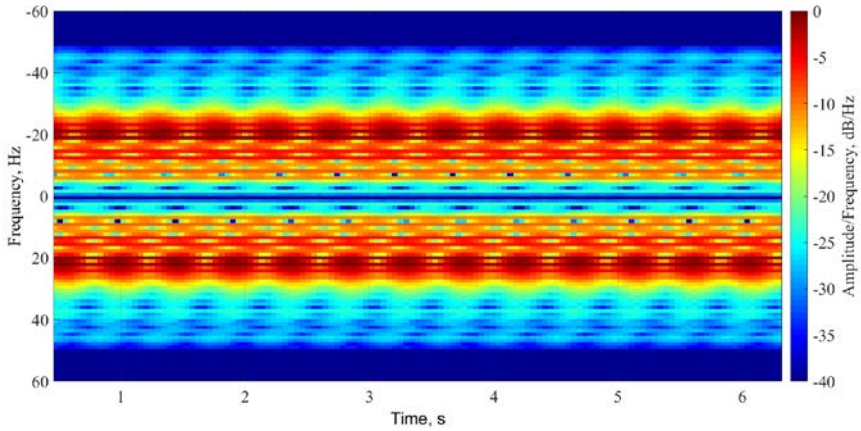

(a)

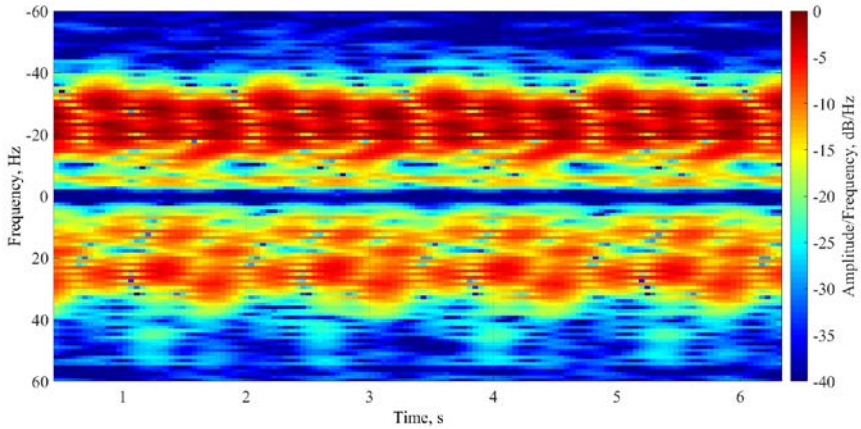

(b)

Fig. 17: Micro-Doppler signature of the full WT with flat blades. (a) Theoretical signature. (b) Experimental signature. Experimental parameters: $l_b \times d_b = 0.50m \times 0.03m$, $Z_N = 0.48m$, $R_N = 3.75m$, , $f_0 = 24GHz$, $\Omega = 4.6$ rad/s

The results presented in the figures above are difficult, if possible at all, to compare to existing experimental results such as those in [12] and [17], as they are focused on monostatic and bistatic measurements in the far-field whereas our results focus on monostatic measurements in the near-field. However, some comments could be made on qualitative aspects of the results obtained here. For example, the theoretical spectrogram of Fig. 17a predicts the same intensity in both upper and lower halves of the graph, as expected from the symmetry of the WT with respect to the vertical axis. If the alignment is not perfect during the measurement, part of the energy is scattered away from the radar in one side of the turbine and towards the radar in the symmetric side. Even if the alignment was perfect, this phenomenon would still be more pronounced if the blades were curved, as will be discussed in more detail in the next section.

C. Results for curved blades

The simulated and experimental time-domain signals of a single curved blade can be seen in Fig. 18. In this case, one of the peaks present in the flat blade signature has disappeared. The reason for that can be attributed to the fact, when curved blades are used, the symmetry of the system is broken. As Fig. 19 sketches, the blade, at the position of maximum reflectivity, does not backscatter the energy in the same direction. Therefore, the received amplitude will decrease when the blade, due to its curvature, scatters energy away from the radar. This phenomenon is predicted by the

theoretical equation (39) with a correlation coefficient of 0.92.

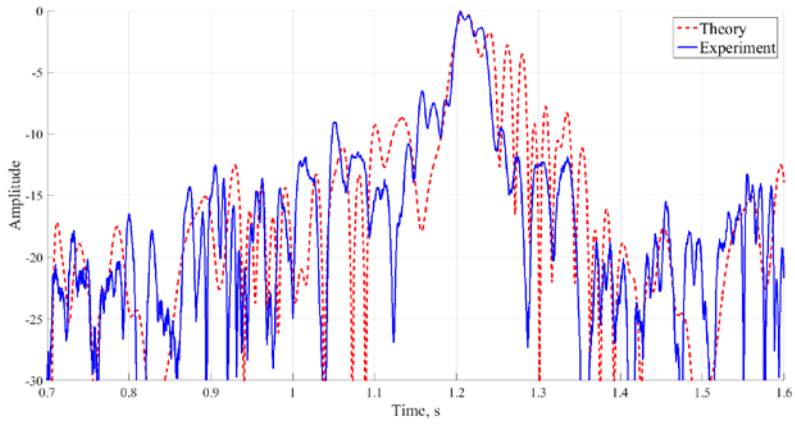

Fig. 18: Comparison between theoretical and experimental time-domain signatures.

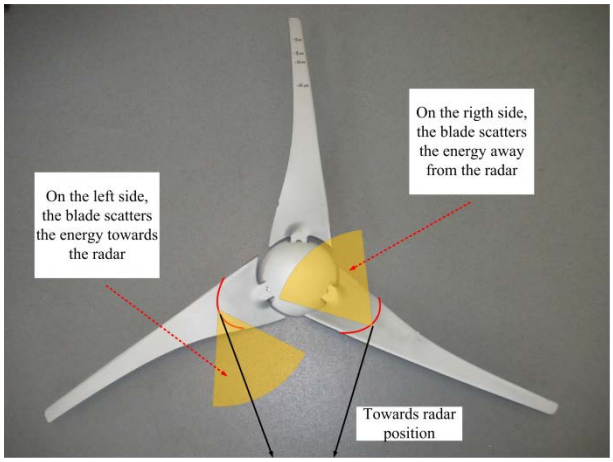

Fig. 19: Schematic mechanism of turbine blade backscatter reflection.

Finally, a comparison between the theoretical and experimental spectrograms is displayed in Fig. 20. The two sides of the experimental micro-Doppler graph differ in the power/frequency levels. This can be explained by the energy scattered away from the radar by the curved blade. The same behavior can be observed in the theoretical signature. An intense response takes place at around $50Hz$ in the experimental spectrogram. This is similar to the case of flat blades. The reason for this is that the moment at which the flash takes place depends on the geometrical parameters of the set-up which were the same in the case of the flat and curved blades.

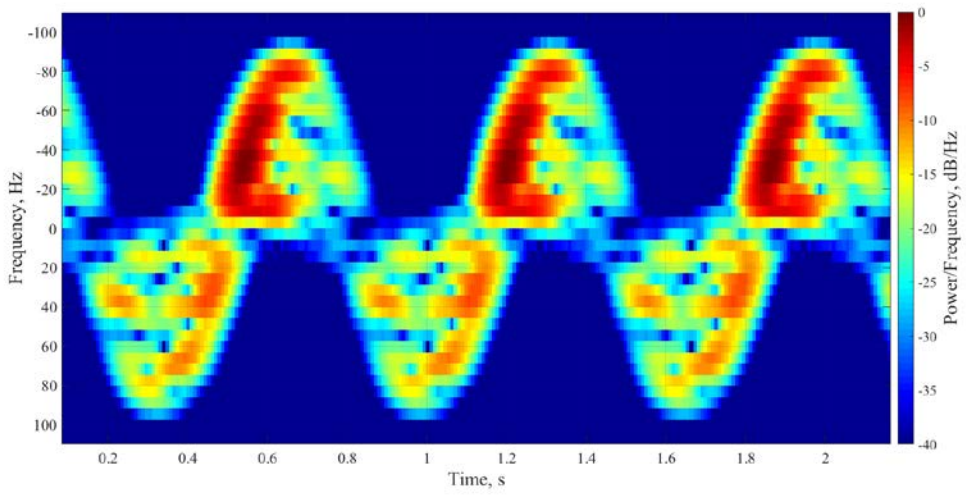

(a)

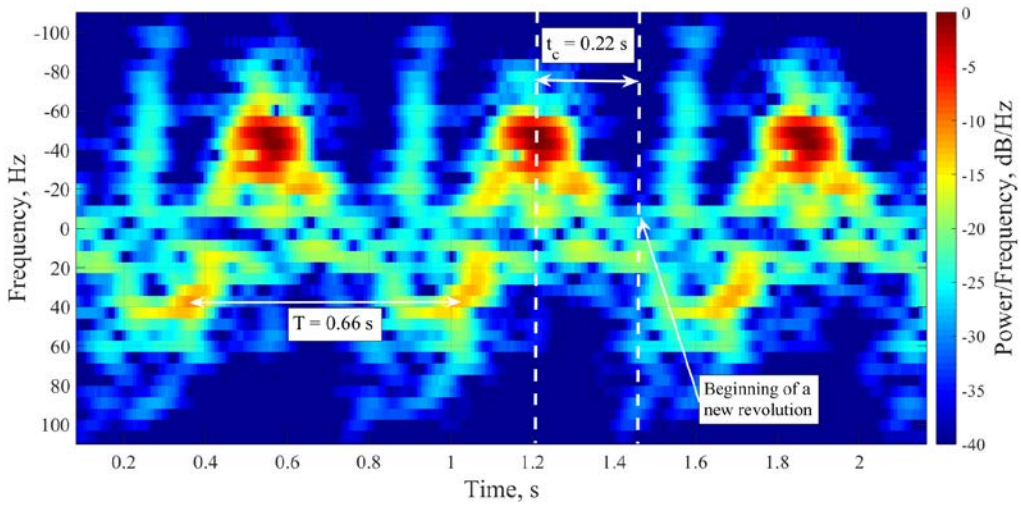

(b)

Fig. 20: Micro-Doppler signature of a single curved blade. (a) Theoretical signature. (b) Experimental signature.

The shape of the spectrograms in Fig. 20 is not as simple as the one corresponding to a flat blade. As it can be seen from equation (8), the amplitude of each frequency will depend in general on the physical parameters of the set-up. The curved shape introduces a complex dependence of these amplitudes on geometrical properties of the blade. Even so, the resemblance between the theoretical and experimental results is clear.

The graphs in Fig. 21 corresponds to the micro-Doppler signature of the full WT. Both the theoretical and experimental spectrograms display a similar pattern. In the experimental case, it is

clear how the pattern replicates itself every $T = \frac{2\pi}{\Omega} = \frac{2\pi}{9.4} = 0.67s$. Again, the separation in time between each individual signal is $T_3 = \frac{2\pi}{3\Omega} = \frac{2\pi}{3 \cdot 9.4} = 0.22s$. The characteristic blade flash can be observed at $75Hz$ in both the theoretical and experimental spectrograms.

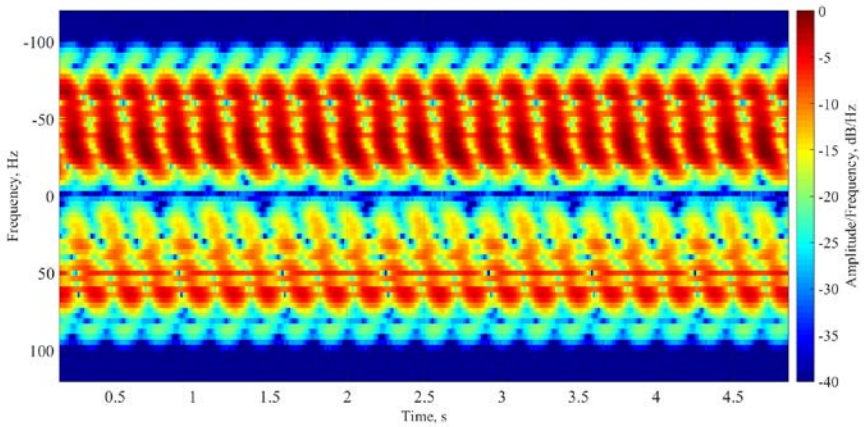

(a)

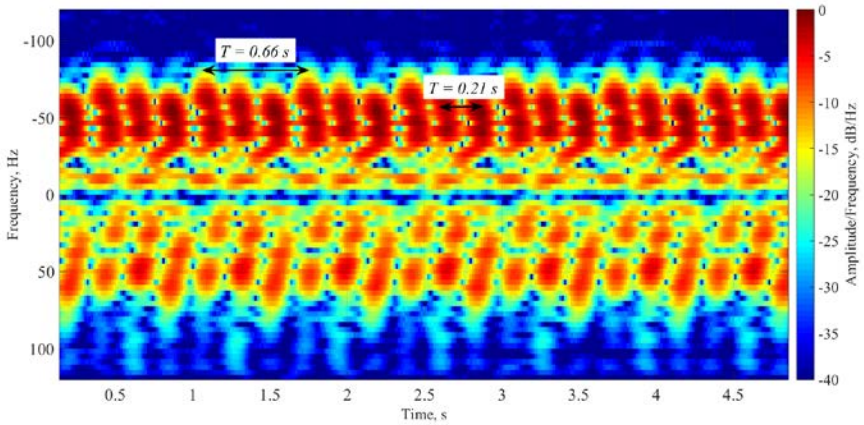

(b)

Fig. 21: Comparison between theoretical and experimental micro-Doppler signatures. Three curved blades. Experimental parameters: $l_b = 0.50m$, $Z_N = 0.48m$, $R_N = 3.70m$, $f_0 = 24GHz$ and Ω=9.4 rad/s.

IV. Conclusions And Future Work

This paper has presented a method of describing wind turbine radar signatures in the near-field. A theoretical model has been developed to characterise radar returns from moving wind turbine blades which can take into account the complexity of their shape. The model was tested in ideal and controlled, but representative experimental conditions within an anechoic chamber, showing a correlation coefficient of ~0.9 between theoretical and experimental results. The good agreement

between theory and experiment confirms the validity of the theoretical framework. It should also be stated here that this work is not limited to WTs, but could potentially be applied to monitoring other rotating objects with short-range radar sensors, such as helicopter rotor blades.

Future work can be split into a number of areas. The natural extension of work reported in this manuscript is to move from the controlled environment of the anechoic chamber to outdoor trials with real wind turbines, to investigate the accuracy of our models in real conditions. In addition, polarimetric acquisitions could be performed to better understand whether there is added value in this extra degree of freedom. Finally, the model developed here can now be used to understand radar signatures of faulty blades in the near-field, and how the corresponding signal properties may be used to diagnose or classify a wind turbine fault using a short-range radar sensor in the vicinity of the turbine blades. In recent published work, the model has been able to accurately describe emulated WT blade faults [30] such as chipped blades, however more work is needed to fully understand the signal properties associated with less straightforward faults such as blade bending.

APPENDIX A

The electric and magnetic field can be obtained through their relations with the vector potential (28). The magnetic field $\vec{B}$ is, in terms of the vector potential,

$$\vec{B}(\vec{r}) = \nabla \times \vec{A}(\vec{r}) \tag{A.1}$$

which is valid everywhere in space.

In order to obtain the expression of the electric field in terms of $\vec{A}(\vec{r})$, Ampere's law can be invoked. Outside the source (where the radar is placed), the rotational of the magnetic field is given by

$$\nabla \times \vec{B}(\vec{r},t) = \mu_0 \left(\vec{J_s} + \varepsilon_0 \frac{\partial \vec{E}(\vec{r},t)}{\partial t} \right) = 0 + \frac{1}{c^2} \frac{\partial \vec{E}(\vec{r},t)}{\partial t} \tag{A.2}$$

The time dependence of $\vec{B}(\vec{r},t)$ and $\vec{E}(\vec{r},t)$ will be the same as the current distribution, that is

$$\vec{B}(\vec{r},t) = \vec{B}(\vec{r}) \cdot e^{-j\omega\left(t-\frac{r}{c}\right)}$$

$$\vec{E}(\vec{r},t) = \vec{E}(\vec{r}) \cdot e^{-j\omega\left(t-\frac{r}{c}\right)}$$

(A.3)

Introducing the previous expressions into (A.2), Ampere's law can be written as

$$\nabla \times \left[\vec{B}(\vec{r}) \cdot e^{-j\omega\left(t-\frac{r}{c}\right)}\right] = \frac{1}{c^2}\frac{\partial}{\partial t}\left[\vec{E}(\vec{r}) \cdot e^{-j\omega\left(t-\frac{r}{c}\right)}\right]$$

(A.4)

The detailed calculations will not be shown in this paper. After manipulating (A.4) and discarding terms that roll off as r^{-1}, because the fields already decay at that rate, the electric field in terms of the magnetic field can be written

$$\vec{E}(\vec{r}) = c\left[\frac{j}{k}\nabla \times \vec{B}(\vec{r}) - \hat{r} \times \vec{B}(\vec{r})\right]$$

(A.5)

where $\hat{r}$ is the unit vector in the direction of the line of sight. The first term in (A.5) simply expresses that an electric field is the source of a magnetic field; this term appears in the case of sinusoidal time-varying targets. The second term can be related to the rotational motion. As the blade rotates, the charge distribution experiences an extra movement that contributes to the variation of the magnetic field and, consequently, the production of an electric field. Both terms present the correct direction of the electric field for plane wave propagation: right angle to the direction of propagation.

Finally, the electric and magnetic fields can be expressed in terms of the vector potential by

$$\vec{B}(\vec{r}) = \nabla \times \vec{A}(\vec{r})$$

(A.6a)

$$\vec{E}(\vec{r}) = c\left[\frac{j}{k}\nabla \times \left(\nabla \times \vec{A}(\vec{r})\right) - \hat{r} \times \left(\nabla \times \vec{A}(\vec{r})\right)\right]$$

(A.6b)

Using the expression obtained for the vector potential in the magnetic field equation:

$$\vec{B}(\vec{r}) = \nabla \times \vec{A}(\vec{r}) = -j\frac{k}{4\pi c\varepsilon_0}\nabla \times \left(\frac{e^{j2kr}}{r}\vec{p}\right) = -j\frac{k}{4\pi c\varepsilon_0}\left[\nabla\left(\frac{e^{j2kr}}{r}\right) \times \vec{p} + \frac{e^{j2kr}}{r}\nabla \times \vec{p}\right]$$

$$= -j\frac{k}{4\pi c\varepsilon_0}\nabla\left(\frac{e^{j2kr}}{r}\right) \times \vec{p}$$

(A.7)

where the fact that the electric dipole does not depend on the observation coordinates is implied. After performing the gradient in (A.7) and keeping only terms of order r^{-1}, the magnetic field becomes

$$\vec{B}(\vec{r}) = \frac{k^2}{2\pi c\varepsilon_0}\frac{e^{j2kr}}{r}\hat{r} \times \vec{p}$$

(A.8)

Similar calculations in the electric field expression (A.6b) produce:

$$\vec{E}(\vec{r}) = \frac{k^2}{2\pi\varepsilon_0}\frac{e^{j2kr}}{r}\left\{\left[2\left(1 - \frac{1}{jkr}\right)(\hat{r} \times \vec{p}) \times \hat{r} - j\frac{1}{kr}[\vec{p} + \hat{r}(\vec{p} \cdot \hat{r})]\right] + (\hat{r} \times \vec{p}) \times \hat{r}\right\}$$

(A.9)

and if only terms that fall of as r^{-1} are conserved

$$\vec{E}(\vec{r}) = \frac{3}{2}\frac{k^2}{\pi\varepsilon_0}\frac{e^{j2kr}}{r}(\hat{r} \times \vec{p}) \times \hat{r}$$

(A.10)

REFERENCES

1. J. Perry and A. Biss (2007, Jul.). Wind Farm Clutter Mitigation in Air Surveillance Radar. IEEE, Radar Conference [Online] 22(7), pp. 93-98. Available: 10.1109/MAES.2007.4285990

2. L. Sergey et al. Advanced Mitigating Techniques to Remove the Effects of Wind Turbines and Wind Farms on Primary Surveillance Radars. Presented at IEEE Radar Conference. [Online]. Available: 10.1109/RADAR.2008.4721114

3. Gavin J. Poupart, "Wind Farms Impact on Radar Aviation Interests - Final Report", QinetiQ, UK. FES W/14/00614/00/REP. 2003

4. Gallardo-Hernando, B. et al. (2011, Feb.). Wind turbine clutter observations and theoretical validation for meteorological radar applications. IET Radar, Sonar & Navigation [Online] 5(2), pp. 111-117. Available: http://dx.doi.org/10.1049/iet-rsn.2009.0296

5. Gallardo-Hernando, B. et al. (2010, Aug.). Detection and Mitigation of Wind Turbine Clutter in C-band Meteorological Radar. IET Radar, Sonar & Navigation [Online] 4(4), pp. 520-527. Available: http://dx.doi.org/10.1049/iet-rsn.2008.0212

6. Gallardo-Hernando, B. et al. (2011, Dec.), Super-resolution techniques for wind turbine clutter spectrum enhancement in meteorological radars. IET Radar, Sonar & Navigation [Online] 5(9), pp. 924-933. Available: http://dx.doi.org/10.1049/iet-rsn.2010.0362

7. Aniceto Belmonte and Xavier Fabregas (2010, Jul.). Analysis of Blockage on Doppler Weather Radar Beams. IEEE Antennas and Wireless Propagation Letters [Online] 9. pp. 670-673. Available: 10.1109/LAWP.2010.2057238

8. Makal Yucedag, S. et al. (2014, Oct.). Analytical method for monostatic radar cross section calculation of a perfectly conducting wind turbine model located over dielectric lossy half space. IET Radar, Sonar and Navigation [Online] 8(8), pp. 965-970. Available: http://dx.doi.org/10.1049/iet-rsn.2014.0055

9. Danoon, L. R. et al. (2013, Oct.). Modeling Methodology for Computing the Radar Cross Section and Doppler Signature of Wind Farms. IEEE Transactions on Antennas and Propagation [Online] 61(10), pp. 5166 – 5174. Available: 10.1109/TAP.2013.2272454

10. B. M. Kent, K. C. Hill, A. Buterbaugh, G. Zelinski, R. Hawley, L. Cravens, et al., "Dynamic Radar cross section and radar Doppler measurements of commercial General Electric windmill power turbines - Part 1: predicted and measured radar signatures," IEEE Antennas and Propagation Magazine, vol. 50, pp. 211-219, 2008.

11. Balleri A. et al. (2013, Feb.). Measurements and analysis of the radar signature of a new wind turbine design at X-band. IET Radar, Sonar & Navigation [Online] 7(2), p. 170 – 177. Available: http://dx.doi.org/10.1049/iet-rsn.2012.0026

12. Ritchie, M. et al. (2015, Jul.). Measurement and analysis of multiband bistatic and monostatic radar signatures of wind turbines. Electronics Letters [Online] 51(14), pp. 1112-1113. Available: http://dx.doi.org/10.1049/el.2015.0856

13. R. Rudd and B. Rhandawa, “RCS Measurement of Wind Turbines”, in Antennas and Propagation, EuCAP 2009, Berlin, 2009, pp. 3642-3644

14. Pinto, J. et al. (2010, Feb.). Stealth Technology for Wind Turbines. IET Radar, Sonar & Navigation [Online] 4(1), pp. 126-133. Available: http://dx.doi.org/10.1049/iet-rsn.2009.0031

15. A. Buterbaugh, B. M. Kent, K. C. Hill, G. Zelinski, R. Hawley, L. Cravens, et al., "Dynamic radar cross section and radar Doppler measurements of commercial General Electric windmill power turbines - Part 2: predicted and measured Doppler signatures," 2007 Antenna Measurements Techniques Association (AMTA) Symposium, St Louis, MO, USA.

16. F. Kong, Y. Zhang, and R. D. Palmer, "Wind turbine radar interference studies by polarimetric measurements of a scaled model," IEEE Transactions on Aerospace and Electronic Systems, vol. 49, pp. 1589-1600, 2013.

17. Fioranelli, F; Ritchie, M; Griffiths, H; Balleri, A, "Analysis of multiband monostatic and bistatic radar signatures of wind turbines," 2015 IEEE Radar Conference, pp.277-282, 27-30 Oct. 2015, Johannesburg, RSA.

18. de Wind, H.J.; Kloke, K.H.; Boniger, U.; Pratisto, H., "Comparison of the recorded RCS and spectra of three different wind turbines on L- and S-band," 2015 IEEE Radar Conference, pp.266-271, 27-30 Oct. 2015, Johannesburg, RSA.

19. Nai, Feng et. al. (2013, Feb.). On the mitigation of wind turbine clutter for weather radars using range-Doppler spectral processing. IET Radar, Sonar and Navigation [Online] 7(2), pp. 178-190. Available: http://dx.doi.org/10.1049/iet-rsn.2012.0225

20. Yimin Zhang et al., “On the effects of rotating blades on DS/SS communication systems”, IEEE Statistical Signal and Aray Processing (SSAP 2000), 2000, pp. 682-686

21. Karabayir O. et al. (2013, Feb.). Wind turbine signal modelling approach for pulse Doppler radars and applications. IET Radar, Sonar & Navigation [Online] 9(3), pp. 276 – 284. Available: http://dx.doi.org/10.1049/iet-rsn.2014.0094

22. C.A. Jackson and M. M. Butler, “Options for Mitigation of the Effects of Wind Farms on Radar Systems”, in IET International Conference on Radar Systems, Edinburgh, UK, 2007, pp. 1-6

23. T. Quilter and M. Jahangir. (2014, Sept.). Performance of 3D non-scanning array to detect targets in the presence of wind turbines- A step change for air traffic control. [Online]. Presented at Tyrrhenian International Workshop on Enhanced Surveillance of aircraft and vehicles. Available: 10.1109/TIWDC-ESAV.2014.6945460

24. “Pure Power: Wind energy targets for 2020 and 2030”, European Wind Energy Association, July 2011

25. P. Tavner, “Offshore wind turbines: Reliability, availability and maintenance”, IET Renewable Energy Series 13, 2012

26. Ki-Yong Oh et al. (2014, Aug.). Blade health monitoring and diagnosis method to enhance operational safety of wind turbine. Presented at Conference on Precision Electromagnetic Measurements (CPEM 2014) [Online]. Avialable: 10.1109/CPEM.2014.6898385

27. Jiabiao Ruan et al. (2014, Apr.). Structural health monitoring of wind turbine blade using piezoceremic based active sensing and impedance sensing. Presented at IEEE 11th International Conference on Networking, Sensing and Control (ICNSC) [Online]. Available: 10.1109/ICNSC.2014.6819704

28. Ki-Yong Oh et al. (2015, Jun.). A Novel Method and its Field Tests for Monitoring and Diagnosing Blade Health for Wind Turbines. Presented at IEEE Transactions on Instrumentation and measurement [Online]. Available: 10.1109/TIM.2014.2381791

29. B. F. Sorensen et. al, “Fundamentals for remote structural health monitoring of wind turbine blades”, RisØ National Laboratory, Roskilde, Denmark, Risø-R-1336(EN), 2002

30. M. Crespo-Ballesteros and M. Antoniou (2015, May). Automatic classification of wind turbine structural faults using Doppler radar: proof of concept study. 2015 IEEE Radar Conference (RadarCon) [Online]. Available: 10.1109/RADAR.2015.7131011

31. Yan Zhang et al. (2011, April). Using Scaled Models for Wind Turbine EM Scattering Characterization Techniques and Experiments. IEEE Transactions on Instrumentation and measurement [Online] 60(4), pp. 1298-1306. Available: 10.1109/TIM.2010.2085271

32. H. Trzaska, “The Near-Field and the Far-Field,” in Electromagnetic Field Measurements in the Near Field, 2 nd ed., Atlanta

33. M. Bryanton et al., Stealth Technologies for Wind Turbines Final Report, BAE, Rep. No: TES101865, Dec. 2007.

34. M. Crespo-Ballesteros and M. Antoniou (2014, Oct.). Wind Turbine Radar Signature Analysis in the Near-Field. Presented at International Radar Conference [Online]. Available: 10.1109/RADAR.2014.7060367

35. B. Boashash, “Heuristic Formulation of Time-Frequency Distributions,” in Time Frequency Signal Analysis and Processing, 2 nd ed., Brisbane

36. V. C. Chen and H. Ling, “Time-Frequency Transforms,” in Time-Frequency Transforms for Radar Imaging and Signal Analysis, 1 st ed., Boston, MA

37. V. C. Chen, “Introduction,” in The Micro-Doppler Effect in Radar, 1 st ed., Boston

38. M. O. Hansen, “3-D Aerodynamics,” in Aerodynamics of wind turbine, 2 nd ed., London, UK

39. Constantine A. Balanis, “Radiation and Scattering Equations”, in Advanced Engineering Electromagnetics, 2nd ed., United States of America

40. J. M. Lee, “The Tangent Structure,” in Manifolds and Differential Geometry, Providence, Rhode Island

41. J. D. Jackson, “Radiating Systems, Multipole Fields and Radiation,” in Classical Electrodynamics, 3 rd ed., United States of America

42. “RFbeam Microwave K-LC2 datasheet,” [Online]. Available: http://www.rfbeam.ch/fileadmin/downloads/datasheets/Datasheet_K-LC2.pdf.